Fundamental Research xxx (xxxx) xxx

Contents lists available at ScienceDirect

Fundamental Research

journal homepage: http://www.keaipublishing.com/en/journals/fundamental-research/

Article

Engineering Electronic Platinum–Carbon Support Interaction to Tame Carbon Monoxide Activation

Wenyao Chen[a,1], Changwei Liu[a,1], Cheng Lian[a,1], Yaxin Yu[a], Xiangxue Zhang[a], Gang Qian[a], Jia Yang[b], De Chen[b], Xinggui Zhou[a], Weikang Yuan[a], Xuezhi Duan[a,*]

[a] State Key Laboratory of Chemical Engineering, East China University of Science and Technology, 130 Meilong Road, Shanghai 200237, China.
[b] Department of Chemical Engineering, Norwegian University of Science and Technology, Trondheim 7491, Norway

ARTICLE INFO

Article history:
Received 24 April 2022
Received in revised form 23 May 2022
Accepted 13 June 2022
Available online xxx

Keywords:
CO activation
EMSI
Reaction pathway
Rate-determining step
de novo strategy

ABSTRACT

CO oxidation has been studied for more than a century; however, molecular-level understanding of its activation protocol and related intermediates remains elusive. Here, we present a unified mechanistic and kinetic picture of various electronic metal–support interactions within platinum–carbon catalysts via in situ spectroscopic/kinetic analyses and multi-scale simulations. Transient kinetic analysis and molecular dynamics simulations with a reactive force field provided a quantitative description of the competition between the oxygen association and oxygen dissociation mechanisms tuned by the interfacial charge distribution and CO coverage. Steady-state isotopic transient kinetic analysis and density functional theory calculations revealed a simultaneous shift in the rate-determining step (RDS) from O_2^* dissociation to O^* and CO^* and O_2^* and CO^* association. A de novo strategy from the interfacial charge distribution to the reaction mechanism, kinetics/thermodynamics of RDS, and, ultimately, catalytic performance was developed to quantitatively map the above CO activation mechanism with an order-of-magnitude increase in reactivity. The proposed catalytic picture and de novo strategy are expected to prompt the development of theories and methodologies for heterogeneous catalysis.

1. Introduction

Rational catalyst design relies on an understanding of the mechanism by which the catalyst operates, and further tailoring of the electronic structure of catalyst surfaces/interfaces has emerged as an excellent strategy to enhance catalytic performance [1–5]. After pioneering work on model catalysts had been reported by both theoretical and surface chemists, considerable progress was achieved in this field, with the energetics of adsorbing species being identified as descriptors for screening catalysts and predicting their functionalities [6,7]. However, challenges associated with the expansion of single-crystal model catalysts to practical nanocatalysts remain. First, the nanocatalyst surfaces/interfaces are usually heterogeneous, and their variable electronic structures arising from the strong electronic metal–support interaction (EMSI) under working conditions could blur the structure–performance relationship [8–10]. Second, the reaction mechanisms are often complicated by competing pathways with multiple products, and the reaction intermediates are considered as "black boxes," that is, their relevance in metal electronic structures is typically neglected [11–13]. Therefore, a combination of advanced characterization techniques [14,15], well-designed in-situ reaction cells, and related kinetic measurement protocols [16,17] is highly desirable to gain a deep understanding of the generation and consequences of EMSI. Particular attention should be focused on the reaction mechanism, rate-determining step (RDS), and intermediates, which dictate the kinetics and thermodynamics of elementary steps to open the "black box."

Herein, we propose a unified picture of the mechanism and kinetics of various EMSIs for CO activation over platinum-carbon catalysts for the first time. Transient kinetic analysis (TKA) and molecular dynamics simulations based on a reactive force field (ReaxFF-MD) were employed to study the competition in the reaction mechanism, and the steady-state isotopic transient kinetic analysis (SSITKA) and DFT calculations were used to investigate the simultaneous shift of RDS. A de novo strategy was developed to quantitatively reveal the generation and consequences of EMSI in CO activation. Consequently, the proposed catalytic picture and de novo strategy are expected to facilitate the development of new theories and methodologies for the investigation of EMSI.

2. Material and methods

2.1. Catalyst preparation

Three carbon materials, i.e., Vulcan XC-72 (Cabot Corporation), carbon nanotubes (CNT, Sigma-Aldrich) and carbon nanofibers (CNF,

* Corresponding author.
E-mail address: xzduan@ecust.edu.cn (X. Duan).
[1] These authors contributed equally to this work.

https://doi.org/10.1016/j.fmre.2022.06.012

Sigma-Aldrich), were used as received to support Pt catalysts by the incipient wetness impregnation method. Typically, calculated amounts of H_2PtCl_6 (≥ 37.5% metal based, Sigma-Aldrich) were dissolved in deionized water and then mixed with catalyst support to obtain 1.0 wt% Pt loading. Then these catalyst precursors were aged at room temperature overnight and dried at 80 ˚C for 12 h. The as-prepared catalysts were reduced by pure hydrogen at 250 ˚C for 2 h, and then passivated with 1% O_2/Ar at room temperature for another 30 min to prohibit bulk oxidation before characterization and testing.

2.2. Catalyst characterization

The specific surface area and total pore volume of the CNT were measured via N_2-physisorption using a Micrometrics ASAP 2020 at -196 ˚C. Raman spectroscopy was performed using a Horiba Jobin Yvon Labram HR instrument. X-ray diffraction (XRD) was performed on a Rigaku D/Max2550VB/PC (Rigaku, Japan, Cu Kα radiation). Thermogravimetric analysis (TGA) was carried out using a Perkin-Elmer STA6000 thermogravimetric analyzer at a heating rate of 10 ˚C·min^{-1} to 800 ˚C under nitrogen atmosphere. The types of surface functional groups on the carbon supports were identified by FTIR on a PerkinElmer Spectrum 100 FTIR spectrometer with samples prepared in the form of potassium bromide pellets. The morphology and structure of catalysts were characterized by a Tecnai G2 F20 S-Twin transmission electron microscope with an accelerating voltage of 200 kV, and an FEI Titan Themis 300 STEM system operating at 200 kV equipped with spherical aberration (Cs) correctors. X-ray photoelectron spectroscopy (XPS) was performed on a Kratos XSAM-800 scanning X-ray microprobe with Al K_α (hυ=1486.6 eV) X-ray as the excitation source. Quasi in situ XPS spectra were recorded on a VG MultiLab 2000 spectrometer with an Omicron Sphera II hemispherical electron energy analyzer with a monochromatic Al K_α X-ray source (1486.6 eV, anode operating at 15 kV and 300 W), in which the constant pass energy and base pressure of the system were set as 40 eV and 5.0×10^{-9} mbar, respectively. The catalysts were treated under the real reaction conditions with elevated temperature in a homemade reaction chamber under ambient pressure, and then transferred to the XPS analysis chamber for XPS measurement through a load-lock gate without exposure to air. The in situ ultraviolet-visible (UV-vis) spectra were recorded using an AVASPEC fiber optical spectrometer (Avantes) equipped with a deep-UV deuterium-halogen light source and a CCD array detector. The in situ Raman spectra were recorded with a back scattering Raman spectrometer (LabRAM HR800, form Horiba JY), using a sample cell under the same reaction conditions. The XAFS spectra at Pt L_3 (E_0 = 11564.0 eV) edge were performed at BL14W1 beamline of Shanghai Synchrotron Radiation Facility (SSRF) operated at 3.5 GeV under the “top-up” mode with a constant current of 240 mA. The XAFS data centers under the fluorescence mode with a Lytle ion chamber. The energy was calibrated accordingly to the absorption edge of pure Pt foil. Athena and Artemis codes were used to extract the data and fit the profiles. For the X-ray absorption near the edge structure (XANES) part, the experimental absorption coefficients as a function of energies μ(E) were processed by background subtraction and normalization procedures, and reported as “normalized absorption” with E_0 = 11564.0 eV for all the tested samples and Pt foil/PtO_2 standard. For the extended X-ray absorption fine structure (EXAFS) part, the Fourier transformed (FT) data in R space were analyzed by applying first shell approximate, PtO_2 and metallic Pt model for Pt-Cl, Pt-O and Pt-Pt contributions, respectively. The passive electron factors, $S_0{}^2$, were determined by fitting the experimental data on Pt foils and fixing the coordination number (CN) of Pt-Pt to be 12, and then fixed for further analysis of the measured samples. The parameters describing the electronic properties (e.g., correction to the photoelectron energy origin, E_0) and local structure environment including CN, bond distance (R) and Debye-Waller factor around the absorbing atoms (σ^2) were allowed to vary during the fit process.

2.3. Catalyst testing

For the determination of the catalytic activity, the as-prepared Pt catalysts were sieved to the particle size of 0.075-0.106 mm before the reaction. Then, 20 mg catalyst was placed on the quartz wool preloaded in the U-shaped reactor. The reaction mixture of 1 vol.% CO, 20 vol.% O_2 and Ar as balance (total flow: 20 ml/min and GHSV: 60000 ml•$g_{cat}{}^{-1}$•h^{-1}) was fed to the initial catalyst. The reaction was studied in the temperature range 25-200 ˚C and atmospheric pressure. The influent and effluent gases were analyzed by an online Agilent 7890 gas chromatograph (GC) equipped with a thermal conductivity detector (TCD).

2.4. (Steady-state isotopic) transient kinetic analysis

20 mg catalyst was preloaded into the U-shaped reactor. The dead volume of the reactor was minimized by filling the voids with quartz wool and a quartz rod to improve the response time of system. Moreover, we used the smooth 1/16” stainless steel tubes, fittings and valves with small dead volumes, and avoided unnecessarily long tubing to minimize the pulse broadening. To initialize the reaction, the catalyst was subjected to a reactant mixture of 1 vol.% CO, 20 vol.% O_2 and Ar as balance with a G.H.S.V. of 60000 ml•$g_{cat}{}^{-1}$•h^{-1}. After the reaction steady-state at 100 ˚C, the feed flow was replaced by a flow of Ar, while keeping the flow rate of Ar before and after the switch. After reaching stable, the feed gas was switched to Ar+$C^{16}O$+$^{16}O_2$ (> 99.9%), Ar+$C^{16}O$+$^{16}O_2$ (50%)/$^{18}O_2$ (50%), and Ar+$C^{16}O$+$^{18}O_2$ (> 97%) with P_{CO}:P_{O2}:P_{Ar}=1:20:79 at the same space velocity of 60000 ml•$g_{cat}{}^{-1}$•h^{-1}. The effluent gas stream was monitored by a TILON LC-D200 mass spectrometer (MS), in which the high sensitivity of MS-based quantification further permits the detection of very low levels of target analytes to minimize the error in transient kinetic analysis. For the steady-state isotopic transient kinetic analysis (SSITKA), the feed flow was replaced by a flow of Kr/^{13}CO/O_2 or Kr/CO/$^{18}O_2$ after the reaction reached steady-state under 100 ˚C and 1.85 bar, while keeping constant the space velocity and the partial pressures of CO and O_2. The effluent gas stream was monitored by a Balzers QMG 422 quadrupole mass spectrometer (MS) and Agilent 7890 gas chromatograph (GC). The data treatment was performed based on our previous study. The average surface residence time of species i, $\tau_{i,measured}$, was determined from the area under the normalized curve:

$$\tau_{i,measured} = \int_0^\infty F_i(t)dt \quad (1)$$

The measured surface residence times were corrected for gas phase holdup, with the use of the inert switching (Ar to Kr). Hence, the average surface residence time, $\tau_{i,corrected}$, was further corrected based on the residence of Ar during the switch:

$$\tau_{i,corrected} = \tau_{i,measured} - \tau_{Ar} \quad (2)$$

Thus, the number of adsorbed species (N_i) could be calculated from the average surface residence time ($\tau_{i,measured}$) and the exit flow ($F_{i,exit}$) of species i:

$$N_i = \tau_{i,corrected} \cdot F_{i,exit} \quad (3)$$

The corresponding surface coverage (θ_i) could be further calculated as:

$$\theta_i = \frac{N_i}{N_{total}} \quad (4)$$

2.5. DFT calculations

All DFT calculations were performed using the Vienna ab initio simulation package (VASP) [18–21] within the generalized gradient approximation (GGA) using Perdew-Burke-Ernzerhof (PBE) functional [22]. The DFT-D3 correction scheme [23] was used to evaluate the weak van der Waals interaction between the adsorbed molecules and the catalyst surface [24]. We used a cutoff energy of 400 eV for Kohn-Sham orbitals,

a Monkhorst-Pack grid for the k-points sampling in the Brillouin zone and a second-order Methfessel-Paxton smearing with a width of 0.05 eV [25]. Considering that the Pt nanoparticles exhibited a main distribution of size between 0.75 nm and 2 nm, the Pt13 cluster with a size of about 0.8 nm was selected to build the metal model, which is one of the most used models in catalysis research due to its higher geometric and electronic stability than other cluster sizes [26]. On the other hand, the multi-layer graphenic network was built as the support to incorporate the effects of surface curvature of these catalysts. Moreover, the singe-layer graphenic network was also built as the support to investigate the effects of the graphite layer. As a result, the Pt13 cluster used for this simulation has cuboctahedral symmetry with one of the four atom facets allowed to interact with support, which would better match the results of EXAFS compared with the icosahedral symmetry. The supported Pt13 cluster models were based on a periodic geometry of 20 Å × 30 Å × 11 Å. A 1 × 1 × 3 Monkhorst-Pack k-point mesh within the surface Brillouin zones was used for these models. In all models, the geometry optimizations were conducted by using a force-based conjugate gradient method [27]. Transition states were computed by means of the dimer method. Convergence of saddle points and minima were believed to reach when the maximum force in each degree of freedom was less than 0.03 eV•Å^{-1}. In order to obtain the atomic charges, a fast algorithm operating on a charge density grid was carried out for Bader charge analysis [28,29]. The charge density difference is calculated as $\rho(r)=\rho_{total}(r)-\rho_{Pt}(r)-\rho_{support}$, where $\rho_{total}(r)$, $\rho_{Pt}(r)$ and $\rho_{support}$ are the charge density of the Pt supported on the support, Pt cluster and support, respectively. The resultant charge density difference is plotted by using VESTA visualization software.

2.6. ReaxFF MD simulations

In this study, reactive force-field molecular dynamics (ReaxFF-MD) were applied to gain a deep insight into the adsorption, chemical reactions, and other mechanical processes of CO oxidation. ReaxFF-based reactive molecular dynamics has been successfully used for simulating heterogeneous catalytic reactions which can describe the chemical reactions in a much wider range of scales than DFT calculations and reproduce the reaction barriers and energies with a greatly reduced computational cost [30–34]. ReaxFF is based on a general distance-dependent bond-order functions relationship introduced by Tersoff [35,36], where the bond formation and fracture are determined by bond orders (BO_{ij}') calculated from interatomic distances. Two systems were modeled as listed in Table S1. The Pt-pri system was modeled with Pt catalyst composed of 2160 carbon atoms and 310 Pt atoms, with 60 CO molecules and 300 O_2 molecules distributed randomly in a box of 80 × 100 × 40 Å with the density of 0.8 g•cm^{-3}. A Pt nanoparticle was created by Atomic Simulation Environment (ASE) software, which first was asked for 6 layers for the {100} surface family, then asked for 5 layers for the {111} family of surfaces. For modeling the supported catalyst, we changed the number of layers for the (-1,1,1) surface to truncate the particle before its center point to form a half cylinder with a radius of 2.7 nm. We used packmol [37,38] to place the Pt310 on the CNT-pri with the minimum clearance between set 2.3Å. Moreover, we modified the carbon atoms of CNT-pri around Pt cluster with 60 hydroxyl groups for Pt-OH simulations to study the effect of hydroxyl on the catalytic process. The Pt/C/H/O ReaxFF force field was used for MD simulations [39], which has been used to study the catalytic mechanisms and kinetics of methane oxidation mixed with Pt/graphene-based nanoparticle additives [40]. The initial configurations of the two structures were minimized using the conjugate gradient (CG) algorithm. Then, during the initialization, each structure was maintained at 300 K for 25 ps before heating it up to 600 K, in 15 ps rapidly. Finally, these systems were equilibrated at the target temperature of 600 K for 500 ps to collect data, because CO could be oxidized almost completely at this temperature and the deformation of Pt nanoparticle was within the acceptable limits. The velocities and positions were updated by the rRESPA multi-timescale integrator, and all MD simulations were performed on canonical (NVT) ensemble using a constant temperature-constant volume, as well as a Berendsen thermostat with a damping constant of 100 fs. A time step of 0.25 fs for 2×10^6 iterations (up to 0.5 ns) was assigned because 0.25 fs described the reactions of CO and O_2 molecules on Pt nanoparticles efficiently. All the ReaxFF MD simulations were performed using the REAXC package embedded in LAMMPS (Large-scale Atomic/Molecular Massively Parallel Simulator) software [41,42].

3. Results and discussion

3.1. (In situ) characterization of the EMSI

The textural properties of the three carbon supports were characterized by N_2-physisorption, and the results are summarized in Table S2. The abundant surface defects and oxygen-containing groups (OCGs) of the carbon supports (VXC, CNT, and CNF) were employed as ligands to manipulate the platinum–carbon interactions. The Raman spectra in Fig. S1 exhibit two prominent peaks at approximately 1347 (D1) and 1583 cm^{-1} (G), which are ascribed to the activation of the breathing mode of the carbon rings of A1g symmetry at the edge of the graphite planes and the in-plane stretching mode of E2g symmetry at sp_2 sites, respectively [43]. Thus, the ratio of the D1 band to the G band, I_{D1}/I_G, was calculated as 1.77, 1.38, and 1.81 for VXC, CNT, and CNF, respectively, to quantify the surface disorder and defect level. The X-ray diffraction (XRD) patterns in Fig. S2 exhibit the diffraction peaks of C(002) and C(100) at 2θ angles of approximately 26.0° and 43.5°, which correspond to the periodicity between graphene layers and that within the graphene layer, respectively. Therefore, the low peak intensity, high peak broadening, and negative shift of C(002) from 26.0° to 25.0°, as well as the fluctuant diffraction pattern on the side below 15° for VXC, indicated amorphous and disordered features; these results were in accordance with their low crystallinities in the Raman spectra. The X-ray photoelectron spectroscopy (XPS) O 1s spectrum in Fig. S3 was deconvoluted into carbonyl (531.1 eV), hydroxyl (532.2 eV), ester (533.4 eV), and carboxyl (534.4 eV) groups, which could cause significant resonance and inductive effects on the supported Pt particles.

The structure of the supported Pt particles was characterized by high-angle annular dark-field scanning transmission electron microscopy (HAADF-STEM) in Fig. S4. All catalysts demonstrated homogeneous distributions of Pt particles, which were ascribed to the abundant OCGs and surface defects acting as anchoring sites for metal particle immobilization. The average Pt particle sizes of for Pt/VXC, Pt/CNT, and Pt/CNF were 1.0, 1.1, and 1.1 nm, respectively. Moreover, the single crystallinity of the fcc structure is reflected in the atomic-scale images in Fig. 1a. Moreover, the corresponding fast Fourier transforms (FFTs) and projections showed similar facet exposure of the Pt(111) and Pt(100) facets of the Pt nanoparticles for their equilibrium shapes. Furthermore, Fig. 1b shows the FT Pt L_{III}-edge k^3-weighted EXAFS spectra, and the as-obtained structural parameters are listed in Table S3. Evidently, Pt/VXC and Pt/CNF contained the highest Pt-Pt and Pt-C/O shell fractions, respectively, which agreed with the trend of their OCGs content. Moreover, the total coordination numbers (C.N.) of Pt, including $C.N._{Pt\text{-}Pt}$ and $C.N._{Pt\text{-}C/O}$, were similar for these catalysts, as was consistent with their similar Pt particle sizes. Therefore, although these catalysts vary in the chemical composition of the carbon support, the virtually identical Pt loadings, particle sizes, distributions, and shapes indicate similar geometric structures of Pt particles, which provided a good platform for studying their electronic interactions with carbon supports.

The normalized Pt L_{III}-edge X-ray absorption near edge structure (XANES) profiles in Fig. 1c shows that the white-line (WL) peak increased from Pt/VXC to Pt/CNF, indicating the presence of more unoccupied 5d states of Pt upon bonding or hybridization with OCGs by EMSI [44]. The average partial charges of Pt in terms of its 5d state calculated based on the relationship between the ionic valence and WL intensity of the reference compounds (Pt foil and PtO_2) were +0.85,

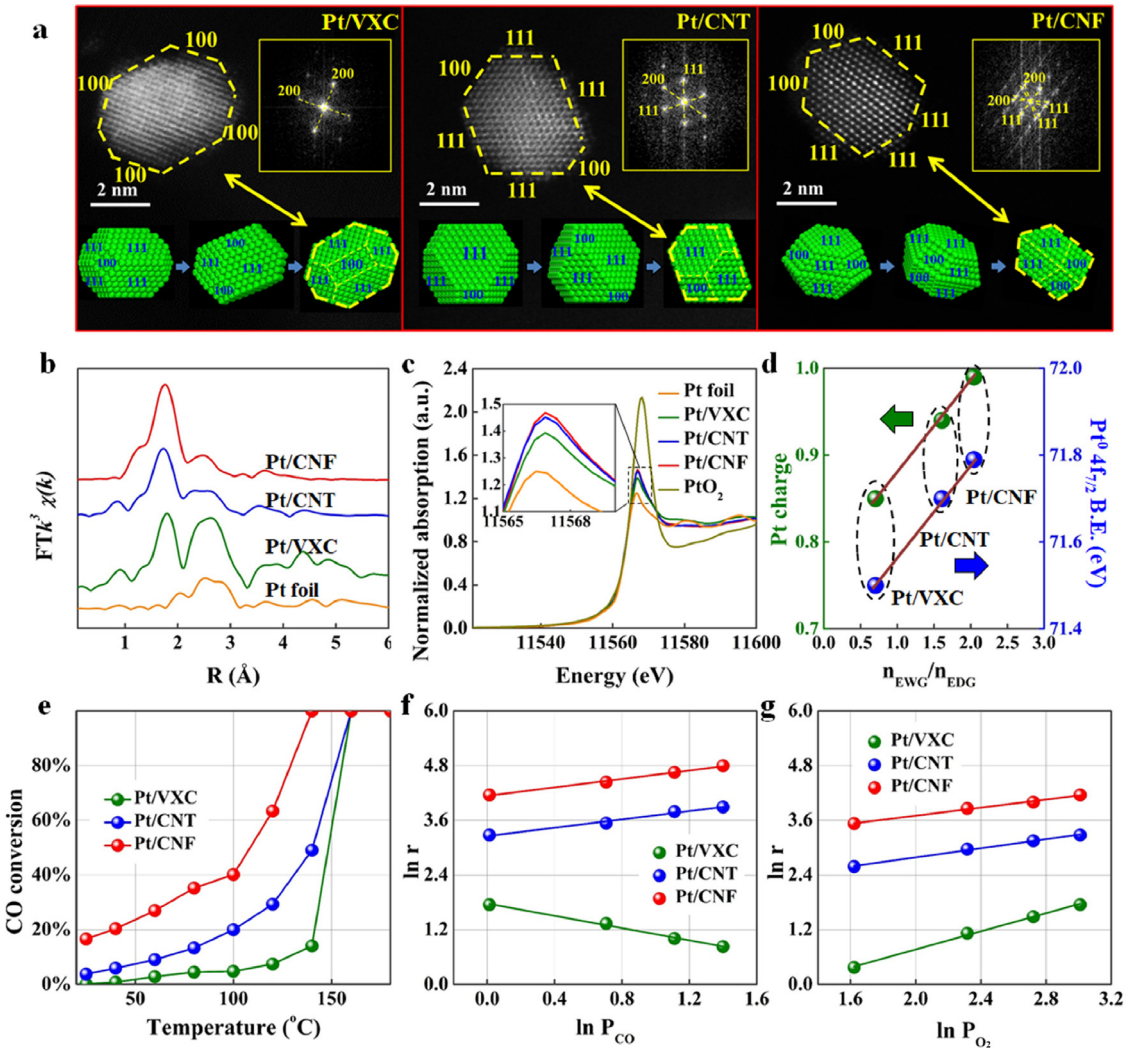

Fig. 1. Characterization of EMSI and kinetic study. (a) Aberration-corrected HAADF-STEM images and the corresponding FFT patterns and projections of truncated octahedron model of Pt/VXC, Pt/CNT, and Pt/CNF. The FT Pt LIII-edge k3-weighted EXAFS (b) and normalized Pt LIII-edge XANES spectra (c) of Pt/VXC, Pt/CNT, and Pt/CNF. (d) Relationships between Pt charge, Pt0 4f7/2 B.E., and nEWG/nEDG. CO conversion as a function of temperature (e) and the kinetic reaction orders of CO (f) and O_2 (g) for Pt/VXC, Pt/CNT, and Pt/CNF.

+0.94, and +0.99, respectively. In general, the changes in valence state by bonding or hybridization between neighboring atoms resulted in a core-level shift, which was further investigated by XPS. The deconvolution of the XPS Pt 4f spectra in Fig. S5 revealed a shift in Pt binding energy (B.E.) from 71.50 eV (Pt/VXC) to 71.70 (Pt/CNT) and 71.79 eV (Pt/CNF). Because the Pt 4f level is not too deep and the wave-function overlap between the Pt 4f and 5d levels is significant, the variation in 5d state occupation number exerts a more pronounced effect on the determination of the B.E. shift than the total number of charges [45]. Consequently, both XANES and XPS analyses confirmed the significant loss of Pt 5d electrons by their transfer to the CNF across the interface. As shown in Fig. 1d, both the Pt charge and B.E. showed virtually linear dependence on the molar ratio of the electron-withdrawing group (EWG) to the electron-donating group (EDG), n_{EWG}/n_{EDG}, which was derived from the OCG contents in Fig. S3. Typically, the electronic effects of the OCGs on the supported metal particles can be categorized into two types: i) resonance effects, which involve the actual movement of electrons through a π-bond system of the carbon support; and ii) inductive effects, which include the polarization of bonds owing to electronegativity differences. Hence, the charge of Pt can be mediated by the electron density of the carbon support and bond polarization based on the electronegativities of the EWG and EDG. EWG decreases the electron density of the metal via resonance (-R) or inductive effect (-I), whereas EDG donates some of its electron density to a conjugated π-system via resonance (+R) or inductive effect (+I). Thus, the interfacial charge distribution can be mediated by the electron density of the carbon support and bond polarization based on the electron affinities of the EWG and EDG (Fig. S6), thereby resulting in linear dependence (Fig. 1d).

Quasi in situ XPS measurements were carried out to trace the evolution of the Pt electronic structures under the reaction conditions. The catalyst was treated in a reaction chamber and then transferred through a load-lock gate to the analysis chamber without exposure to air. As seen in Fig. S7, the Pt^0 4f B.E. remained virtually unchanged until 150°C, beyond which partial oxidation occurred as further verified by the in situ UV-vis spectra in Fig. S8. Moreover, the corresponding in situ Raman spectra (Fig. S9) exhibited negligible shifts in the G band in this temperature range, thereby indicating negligible changes in the electron transfer between Pt and the carbon support. All of these in situ characterizations guaranteed that the above analyses reflect charge transfer via EMSI under a steady state of reaction conditions at relatively low temperatures (less than 150 °C). Furthermore, comparison of the ex situ XPS spectra (Fig. S5) and quasi in situ XPS spectra (Fig. S7) exhibited a slight increase in Pt^{n+} species upon exposure to CO, as discussed in the following section.

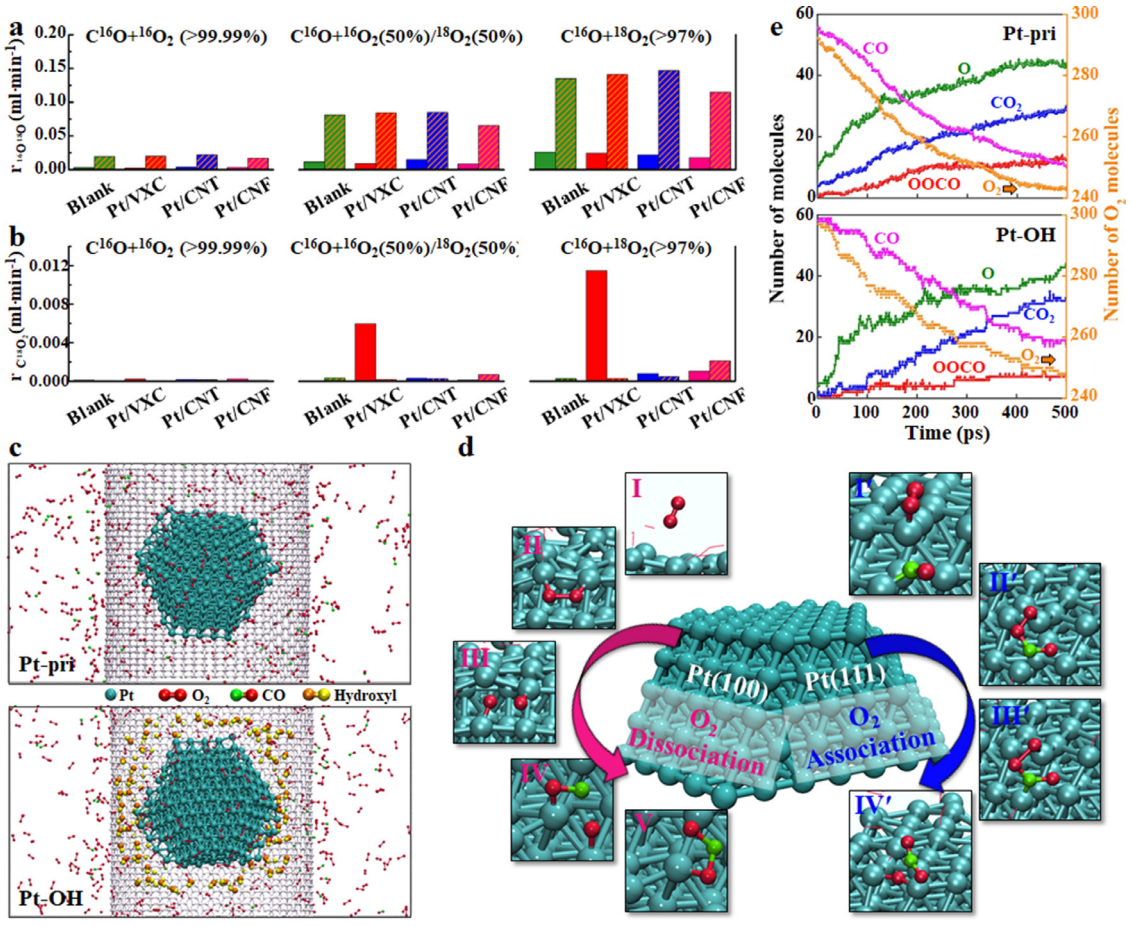

Fig. 2. Dynamic balance of the reaction mechanism. The comparisons of the formation rate of $^{16}O^{18}O$ ($r^{16}O^{18}O$) (a) and $C^{18}O_2$ ($rC^{18}O_2$) (b) between the blank test, Pt/VXC, Pt/CNT, and Pt/CNF, based on the MS data collected during the switch from Ar to Ar+$C^{16}O$+$^{16}O_2$/$^{18}O_2$. The filled and sparsely filled bars correspond to the data after 1 and 5 min of the transient switch, respectively. (c) Initial snapshot of CO oxidation simulation over Pt-pri and Pt-OH. (d) Diagram of CO oxidation mechanisms and the involved snapshots over the Pt(100) and Pt(111) facets. (e) Molecule numbers of CO, O, O_2, OOCO, and CO_2 as a function of simulation time for Pt-pri and Pt-OH.

3.2. Competition of reaction mechanisms

These Pt catalysts were tested in CO oxidation, and the light-off temperature for CO oxidation (Fig. 1e) followed the trend Pt/VXC > Pt/CNT > Pt/CNF. The reaction rates at 100 °C (r_{100}) were 6.3, 26.5, and 53.4 $mmol_{CO}•mol_{Pt}^{-1}•s^{-1}$, further resulting in turnover frequencies of 7.1 × 10^{-3}, 35.8 × 10^{-3}, and 72.2 × 10^{-3} s^{-1}, with Pt/CNF delivering more than 10 times higher catalytic activity than Pt/VXC. Moreover, the three pure supports without metal immobilization were tested for this reaction, demonstrating negligible catalytic activity (CO conversion of less than 1.5% at 100 °C) compared with those of their corresponding supported Pt catalysts. Kinetic studies (Table S4) were conducted by excluding the external and internal diffusion limitations (Supplementary Materials), and the corresponding CO conversion was controlled to less than 15%, except for a few points obtained under 20%, to minimize the influence of mass and heat transfer. As shown in Fig. 1f and 1g, a negative CO reaction order of -0.67 was observed for Pt/VXC, whereas positive values were found for Pt/CNT (0.45) and Pt/CNF (0.46). The O_2 reaction orders for Pt/VXC, Pt/CNT, and Pt/CNF were 1.0, 0.50, and 0.44, respectively. Notably, the first-order dependence of O_2 on Pt/VXC suggests that the catalytic activity is controlled by O_2 adsorption before dissociation or molecular O_2 adsorption because the possibility of a reaction between CO and lattice oxygen or OCGs is disregarded by the following SSITKA. By contrast, higher CO and lower O_2 reaction orders for Pt/CNT and Pt/CNF indicate a weaker CO adsorption.

To understand this change, the reaction mechanism of these catalysts, which was mainly categorized into oxygen dissociation and oxygen association in a previous study [12], was first investigated. Despite numerous publications on the reaction mechanism over Pt-based catalysts, no consensus has been reached because the above two mechanisms yield the same reaction rate equation according to Iglesia et al. [12]. Therefore, although CO oxidation is considered as a "simple" model reaction, its mechanistic details are complex, and their relevance to Pt electronic effects is currently under debate. Thus, identification of the main reaction pathway using transient kinetic analysis (TKA) via isotopic labeling was attempted. Four parallel TKAs (Figs. S10 and S11) were conducted via a transient switch from Ar to Ar+$C^{16}O$+$^{16}O_2$/$^{18}O_2$ at different concentrations. After the transient switch, all samples showed a small amount of $^{16}O^{18}O$, which possibly originated from the impurities in the feed gas $^{18}O_2$ and/or reaction between surface species. In principle, the quasi-equilibrated dissociation of equimolecular $^{16}O_2$/$^{18}O_2$ mixtures yields binomial isotopologue distributions (50% $^{16}O^{18}O$), whereas molecular adsorption steps do not form mixed $^{16}O^{18}O$ isotopes. Thus, the formation rates of the $^{16}O^{18}O$ isotopologue (r_{16O18O}) are compared in Fig. 2a. Evidently, r_{16O18O} monotonously increased with $^{18}O_2$ pressure at either 1 or 5 min; this result was inconsistent with quasi-equilibrated O_2 dissociation. By comparison, the trend of r_{16O18O} for the catalysts was in line with that of the blank test, strongly suggesting that $^{16}O^{18}O$ originated from the isotopologue in the $^{18}O_2$ feed gas.

On the other hand, the concentration of $C^{16}O^{18}O$ also increases with the partial pressure of $^{18}O_2$ as a result of the reaction between $C^{16}O$

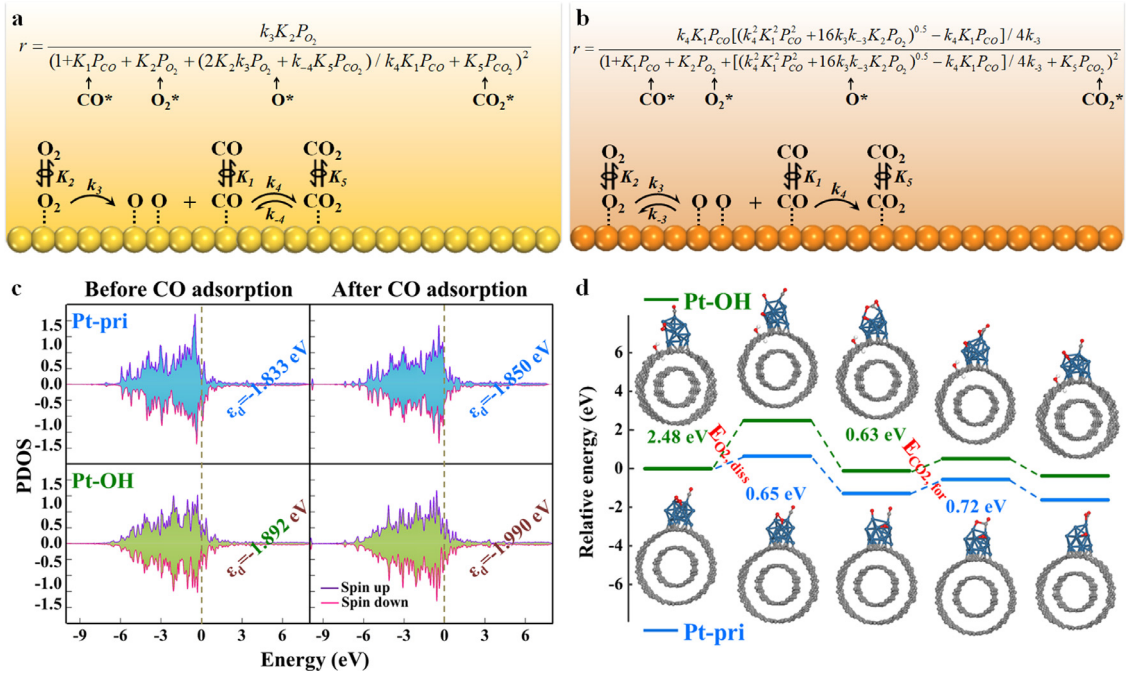

Fig. 3. Dynamic shift of the rate-determining step (RDS). The reaction pathways and rate equations based on O_2 (θO_2), O (θO), and CO (θCO) determined by SSITKA for CO oxidation over Pt/VXC (a), Pt/CNT, and Pt/CNF (b). (c) PDOS analysis of Pt 5d states before and after CO adsorption for Pt-pri and Pt-OH. The vertical dotted line denotes the Fermi level. (d) Potential energy diagram and the corresponding optimized configurations of all reaction intermediates involved in the DFT calculations.

and $^{18}O_2$, and that between $C^{16}O$ and the isotopologue $^{16}O^{18}O$ also gives a small amount of $C^{16}O_2$. Interestingly, Pt/VXC showed a significant amount of $C^{18}O_2$ at 1 min, indicating isotopic exchange within the reaction intermediate (from $^{18}O^*$-^{18}O-C^*-^{16}O to $^{16}O^*$-^{18}O-C^*-^{18}O) via oxygen association instead of oxygen dissociation (Fig. S12). Therefore, more negatively charged Pt possibly allowed the back-donation of more electrons to the CO 2p orbitals during the transient adsorption of CO [46], evidenced by the slightly increased Pt^{n+} percentage under working conditions. As expected, this instant electron back-donation by Pt during the transient adsorption of CO resulted in a short-lived precursor state for oxygen association. However, as shown in Fig. 2b, the formation rate of $C^{18}O_2$ (r_{18O2}) for Pt/VXC gradually decreases to a minimum after reaching a steady state (5 min). Therefore, the instant electron back-donation of negatively charged Pt to CO during the transient adsorption of CO stimulates its association with O_2, whereas the charge relocation of Pt with increased CO coverage in the steady state facilitates O_2 dissociation. Moreover, the mechanism via oxygen dissociation also dominates the steady reaction for Pt/CNT and Pt/CNF in parallel with a small proportion of oxygen dissociation, as evidenced by the low formation rate of $C^{18}O_2$.

Notably, the dominant oxygen-dissociation mechanism is opposite to that in our previous study, in which Pt within a higher B.E. range of 71.85–71.90 eV facilitated the oxygen association mechanism [47]. In this regard, we resorted to the ReaxFF MD simulation by comparing Pt supported on pristine CNT (Pt-pri) and its hydroxyl-incorporated counterpart (Pt-OH) in Fig. 2c, which Bader charge analysis results suggested to be charge deficient and charge rich (Fig. S6), respectively. CO oxidation proceeded in parallel with the oxygen association and dissociation mechanisms for the two models. As shown in Fig. 2d, oxygen association via the formation of OOCO species only occurred on the Pt(111) facet rather than on the Pt(100) facet, whereas oxygen dissociation mainly occurred on the Pt(100) facet. Taking the Bader charge values of -0.052e for Pt(100) and +0.046e for Pt(111) surfaces (Fig. S13), the charge-rich Pt(100) regions enhanced charge transfer to the O_2 molecule and helped weaken the O-O bond for dissociation [48]; this trend was opposite to that for charge-deficient Pt(111) regions. Fig. 2e shows the changes in the molecular number of the reaction species. Evidently, Pt-pri exhibited higher activity for CO conversion compared to Pt-OH, as was consistent with the higher activity of positively charged Pt/CNF. Interestingly, Pt-pri demonstrated a sharp increase in OOCO concentration, which was in line with the trend that positively charged Pt(111) facilitated the oxygen association mechanism. These insights further explain Fig. 2b, which shows that the proportion of oxygen dissociation decreases with Pt partial charge and is compensated by an increase of proportion of oxygen association. Therefore, instead of a single mechanism reported in numerous studies, the mechanisms of oxygen dissociation and oxygen association are in competition, tuned by the interfacial charge distribution and CO coverage for CO activation. Specifically, the positively charged Pt with low CO coverage during its transient adsorption facilitates oxygen association, whereas the negatively charged Pt with high CO coverage under steady state directs CO activation to the oxygen dissociation.

3.3. Dynamic shift of the rate-determining step (RDS)

By applying the pseudo-steady-state approximation to oxygen species (Supplementary Materials), the dissociation of O_2 was determined to be the irreversible step, yielding the rate equation in Fig. 3a for Pt/VXC; by contrast, the association between CO^* and O^* was the irreversible step for Pt/CNT and Pt/CNF, yielding the rate equation in Fig. 3b. Moreover, parity plots (Fig. S14), which were based on the statistical fitting parameters (Table S5) for the abovementioned rate expressions using regressive analysis, exhibited reasonable agreement between the predicted and experimental reaction rates and validated the above kinetics models. To further verify the results, SSITKA was conducted to obtain in situ kinetic (site coverage of the reaction species and rate constant of the elementary step) and thermodynamic parameters (activation enthalpy and entropy) under steady state, as schematically depicted in Fig. S15. An $Ar/^{12}CO$-$Kr/^{13}CO$ switch (Fig. S16) suggested the lowest CO adsorption/desorption for Pt/VXC in Table S6; on this basis, the Pt particle sizes for Pt/VXC, Pt/CNT, and Pt/CNF were determined to be 1.3, 1.1, and 1.1 nm, respectively. Clearly, the particle size

for Pt/VXC as determined by ^{12}CO-^{13}CO switches slightly exceeded that as determined by HAADF-STEM. This result was ascribed to the occurrence of a certain degree of irreversible CO adsorption, as observed by the negative reaction order of CO for Pt/VXC.

Here, Fig. S17 shows the ^{12}CO response curves by switching from Ar/$^{12}CO/O_2$ to Kr/$^{13}CO/O_2$ under steady state. Based on these curves, the amount of adsorbed ^{12}CO (N_{CO}) and its site coverage (θ_{CO}) can be calculated as shown in Table S6. The results show that Pt/CNF has the lowest CO site coverage among the catalysts. Meanwhile, the $^{16}O_2$ site coverage (θ_{O2}) was determined by switching from Ar/CO/$^{16}O_2$ to Kr/CO/$^{18}O_2$. As seen in Fig. S18, the $^{16}O_2$ response curves were almost identical to those of Ar, indicating that the amount of adsorbed $^{16}O_2$ and its site coverage (θ_{O2}) were under the detection limit. Moreover, owing to the insignificant CO_2 readsorption effect (Fig. S19), the CO_2 site coverage (θ_{CO2}) was calculated from the $C^{16}O_2$ response curves (Fig. S20). This value further yielded the oxygen site coverage (θ_{Oxygen}) owing to the large excess of CO on the catalyst surface. The results in Table S6 suggest that Pt/VXC has the highest θ_{CO} and lowest θ_{Oxygen}, as is consistent with irreversible O_2 dissociation, in which the dissociated oxygen can be rapidly consumed by CO. By contrast, Pt/CNT and Pt/CNF exhibit slightly higher θ_O values of 0.03 and 0.07, respectively; these results are consistent with the reversible step of O_2 dissociation before the irreversible step of CO_2 formation. Therefore, accompanying the charge transfer from Pt to the carbon supports, these catalysts possibly underwent a shift in RDS from O_2^* dissociation (Fig. 3a) to CO^* and O^* association (Fig. 3b), thereby resulting in the accumulation of oxygen species on their surfaces. This result explains the observation by Iglesia et al. that a small decrease in θ_{CO} induces a significant decrease in the energy barrier for O_2 dissociation [12].

To gain a deeper understanding of the results, DFT calculations were further carried out by comparing the reaction over the Pt13 cluster supported on pristine substrate (Pt-pri) and its hydroxyl-incorporated counterpart (Pt-OH) as shown in Fig. S21; in the cluster, the dangling bond is terminated with a pseudo-hydrogen atom to maintain the bulk coordination environment. The charge population by integrating the projected density of state (PDOS) up to the Fermi level in Fig. 3c was 7.81 and 8.13 e for Pt-pri and Pt-OH, respectively. Moreover, the d-band was slightly broadened for Pt-OH, leading to a downshift in the d-band center from -1.833 eV to -1.892 eV. Therefore, the hydroxyl group serves as a ligand to tailor the d-state of Pt by increasing the charge population of Pt 5d states as well as downshifting the Pt d-band center. Correspondingly, Fig. 3d shows the energy diagrams of CO oxidation with the optimized atomic configuration. The energy barriers for O_2 dissociation ($E_{O2,diss}$) were calculated as 0.65 and 2.48 eV, whereas those for CO_2 formation ($E_{CO2,for}$) were 0.72 and 0.64 eV for Pt-pri and Pt-OH, respectively. Interestingly, Pt-OH exhibited a much higher energy barrier for O_2 dissociation and lower energy barrier for CO_2 formation than those of Pt-pri; a similar tendency was observed for Pt supported on a single-layer substrate (Fig. S22). Thus, the incorporation of hydroxyl groups increased the interfacial charge transfer to fill the Pt 5d states and reversed the energy barriers for these two steps, resulting in the dynamic shift of the RDS.

Moreover, the downshift of the metal d-band center weakens the adsorption of the adsorbate. For the elementary step of O_2 dissociation, the d-band center downshift of Pt-OH can result in weak O_2 adsorption, as evidenced by the lower site coverage of O_2 in SSITKA, and, consequently, an increased activation energy barrier. However, for the elementary CO_2 formation step, the d-band center downshift can weaken CO adsorption to alleviate the CO poisoning effect and thus decrease the activation energy barrier. This result is attributed to the weak interaction of Pt with O_2 inhibiting the cleavage of the O-O bond in O_2 dissociation, whereas the strong interaction with CO + O inhibits the diffusion of O and CO to form CO_2. Therefore, a compromise of Pt d-band center instead of an excessively high or low value is highly desirable to achieve a trade-off between these two elementary steps, which accounts for the increased $E_{O2,diss}$ and $E_{CO2,for}$ for Pt-OH and Pt-pri, respectively. Notably, the moderate Pt d-band center did not match the concept reported in many studies, which suggest that a lower Pt d-band center better facilitates CO oxidation. These insights provided an in-depth understanding of the experimental observation of the RDS shift by varying the interfacial charge distribution.

Furthermore, the PDOS values of Pt before and after CO adsorption were compared because CO was the most abundant surface intermediate (MASI) in SSITKA. As shown in Fig. 3c, CO adsorption, which is described by electron donation from the CO 5s orbital to the Pt 5d states along with back-donation from Pt 5d states to the CO 2p antibonding orbital [46], induces negative shifts of the d-band center of -0.017 and -0.098 eV for Pt-pri and Pt-OH, respectively. Hence, the larger shift of the d-band center for Pt-OH indicates greater charge transfer between the Pt and CO molecules, which explains the negatively charged Pt/VXC facilitating the oxygen-association mechanism during the transient adsorption of CO by instant charge transfer. Moreover, compared to Pt-pri, Pt-OH can form stronger interactions with CO because of the greater charge transfer between Pt and CO molecules, which account for the higher CO coverage of Pt/VXC in SSITKA. Based on this discussion, the interfacial charge distribution is identified as a motif for the above competition between the reaction mechanisms and the dynamic shift of RDS.

3.4. De novo mapping CO activation

According to the site coverages and rate equation, the rate constant (k) values of RDS was determined to be 1.73 and 1.86 s^{-1} for Pt/CNT and Pt/CNF, respectively. Moreover, considering the negligible changes in reaction order (Fig. S23) and similar adsorption energies in high CO and low O_2 coverages [12], the θ_{CO} and θ_O can be assumed to be unchanged to simplify the following kinetic analysis. Given the activation energy (E_a) values of 20.7 and 12.9 kJ•mol^{-1} (Fig. S24), the frequency factor (A) values were calculated as 1370.2 and 119.1 s^{-1}. The changes in Gibbs function, enthalpy, and entropy between the transition (OCO^*) and ground states (CO^*+O^*) are represented by the Gibbs free energy of activation ($\Delta G^{\dagger}$), activation enthalpy ($\Delta H^{\dagger}$), and activation entropy ($\Delta S^{\dagger}$), respectively:

$$K_C^{\dagger} = RTK_P^{\dagger} = RTexp\left[\frac{\Delta H^{\dagger} - T\Delta S^{\dagger}}{RT}\right] \tag{5}$$

where RT represents a term that accounts for units of the equilibrium constant. Moreover, the relationship between K_c and K_p can be implicitly written as:

$$\begin{aligned} K_C &= K_P RT = \frac{(q^o_{OCO}/N^o RT)}{(q^o_{CO}/N^o RT)(q^o_O/N^o RT)} exp\left[-\frac{\Delta H^o_{r,0K}}{RT}\right] \\ &= \frac{(q^o_{OCO}/V^o)}{(q^o_{CO}/V^o)(q^o_O/V^o)} exp\left[-\frac{\Delta H^o_{r,0K}}{RT}\right] \end{aligned} \tag{6}$$

where q^o is the change in the vibrational partition function. Assuming a molecular partition function per unit volume as z_i gives:

$$z_i = q^o/V^o = \left(\frac{2\pi m k_B T}{h^2}\right)^{3/2} \left(q_{vib} q_{rot} q_{elec}\right) \tag{7}$$

Substituting Eq. 7 into Eq. 6 gives:

$$K_C = \frac{z^{\dagger}_{OCO}}{z_{CO} z_O} exp\left(-\frac{\Delta H^o_{r,0K}}{RT}\right) \tag{8}$$

Based on the Eyring equation, the rate constant for bimolecular reactions can be written as:

$$\begin{aligned} k &= \kappa \frac{k_B T}{h} \frac{z^{\dagger}_{OCO}}{z_{CO} z_O} exp\left(-\frac{E_{0,f}}{RT}\right) \\ &= \kappa \frac{k_B T}{h} K_C^{\dagger} = \kappa \frac{k_B T}{h} RT exp\left(-\frac{\Delta H^{\dagger} - T\Delta S^{\dagger}}{RT}\right) \end{aligned} \tag{9}$$

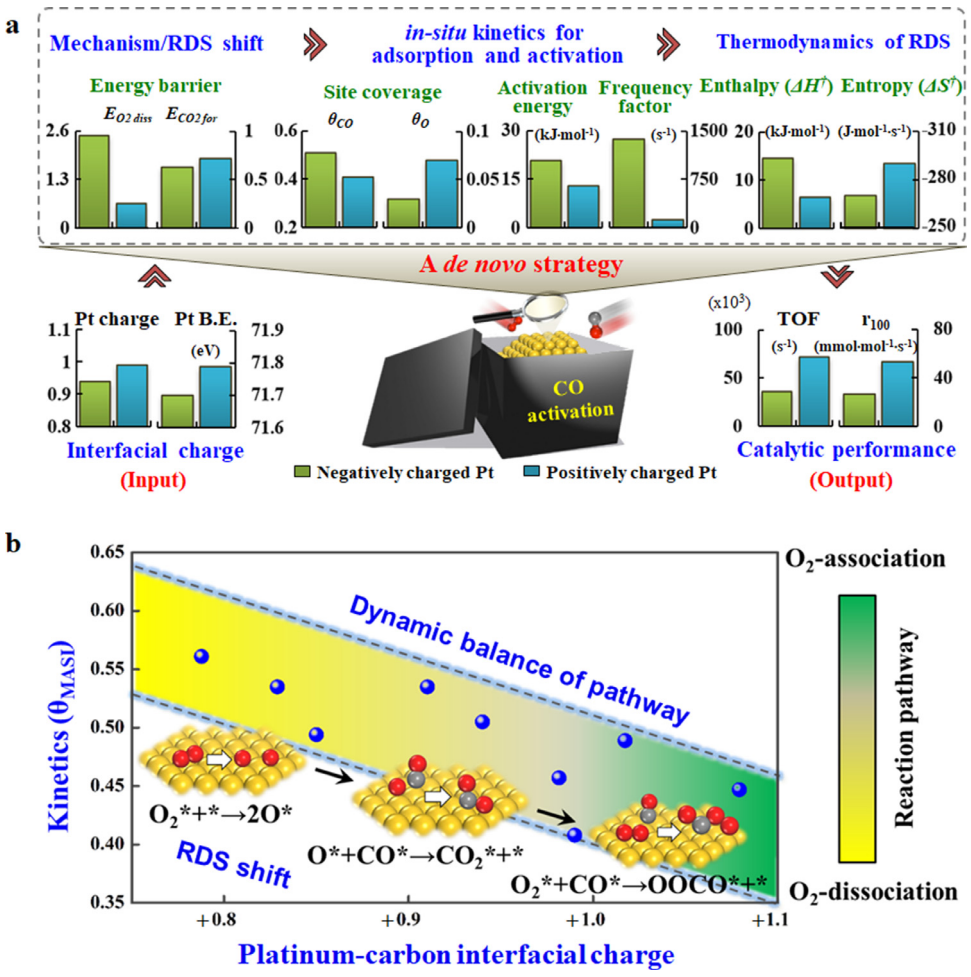

Fig. 4. De novo strategy to map CO activation. (a) The diagram of the de novo strategy to map the EMSI-mediated CO activation. (b) The catalytic picture of the mechanism and kinetics of various EMSI for CO activation over platinum–carbon catalysts.

where κ is the transmission coefficient to quantify the probability that the transition state (OCO*) generates a product (CO_2*) instead of reverting back to reactants (CO*+O*). k_B is the Boltzmann constant, and h is the Planck's constant. Taking the derivative of ln k in Eq. 9 and Arrhenius expression (ln k=ln A-E_a/RT) with respect to T and then combining them gives:

$$E_a = RT^2\left(\frac{2}{T} + \frac{\Delta H^{\dagger}}{RT^2}\right) \tag{10}$$

As a result, substituting Eq. 10 into Eq. 9 gives:

$$\Delta S^{\dagger} = Rln\left(\frac{kh}{k_B RT^2}\right) + \frac{\Delta H^{\dagger}}{T} = \left[ln\left(\frac{kh}{k_B RT^2}\right) - 2\right]R + \frac{E_a}{T} \tag{11}$$

Consequently, $\Delta H^{\dagger}$ and $\Delta S^{\dagger}$ of RDS were further calculated as 14.5 and 6.5 kJ•mol^{-1} and -270.2 and -290.5 J•mol^{-1}•K^{-1} for Pt/CNT and Pt/CNF, respectively. More details are shown in the Supplementary Materials. In general, the flexible adaptation of the catalyst structure and electron distribution along the reaction pathway is crucial for minimizing energy and consequently lowering the activation energy. Meanwhile, stabilization of the transition state by the catalyst environment further decreases the activation entropy. Thus, the electronic platinum–carbon interaction increased freedom loss (larger $\Delta S^{\dagger}$) of the reaction intermediates to promote the formation (larger k) of the rigid transition state (OCO*) with significantly lower energy (smaller $\Delta H^{\dagger}$) of the RDS. With these considerations, a de novo strategy was developed to map the EMSI-mediated CO activation in Fig. 4a. By tailoring n_{EWG}/n_{EDG} from 1.47 to 2.08, the decrease in the Pt partial charge gives a lower θ_{CO} of 0.41 and a higher θ_{Oxygen} of 0.07, thereby facilitating CO activation by decreasing E_a from 20.7 to 12.9 kJ•mol^{-1} and A from 1370.2 to 119.1 s^{-1}. CO activation shifts RDS from O_2* dissociation to CO* and O* association and further accounts for significant decrease in $\Delta H^{\dagger}$ from 14.5 to 6.5 kJ•mol^{-1} and that in $\Delta S^{\dagger}$ from -270.2 J•mol^{-1}•K^{-1} to -290.5 J•mol^{-1}•K^{-1} for RDS. Consequently, the increased freedom loss from the ground state to the transition state, together with a decreased energy barrier, contributes to the higher rate constant of RDS and an apparent two-fold increase in r_{100}.

Further incorporation of the structural features of the Pt catalysts in our previous study [47] with those of the current catalysts yields a catalytic mechanistic and kinetic picture shown in Fig. 4b. The mechanism and kinetics of CO activation vary with electronic platinum–carbon interactions. Typically, CO activation proceeds in parallel with oxygen association and oxygen dissociation, indicating a dynamic balance as a function of the interfacial charge distribution and coverage of CO (MASI). The charge-rich region with high CO coverage under steady state can donate more charge to O_2 to weaken the O-O bond and facilitate oxygen dissociation. By contrast, the charge-deficient region with lower CO coverage, particularly during the transient adsorption of CO, diverts the mechanism from CO activation to oxygen association. Interestingly, the decreased CO coverage by charge transfer from Pt to carbon further induces a dynamic shift of the RDS from O_2* dissociation to O* and CO* association, and finally to O_2* and CO* association; this result indicates that a trade-off between elementary steps is achieved. To

the best of our knowledge, this is the first study to draw a full picture of the mechanism and kinetics of CO activation of various EMSIs over platinum–carbon catalysts. The de novo strategy developed in this work can be extended to probe the EMSI in other reactions.

4. Conclusion

In summary, we developed a de novo strategy to quantitatively map a unified picture of the mechanism and kinetics of various EMSIs for CO activation over platinum–carbon catalysts. A combination of in situ spectroscopic/kinetic analysis and multiscale simulation formulates a quantitative description of the reaction mechanism competition between oxygen association and oxygen dissociation, which is tuned by the interfacial charge distribution and CO coverage. The charge-rich interfacial region can donate more charge to O_2 to weaken the O-O bond and facilitate the oxygen dissociation mechanism, whereas the charge-deficient region with low CO coverage, especially during the transient adsorption of CO, diverts CO activation to the oxygen association mechanism. Moreover, a simultaneous shift of RDS from O_2* dissociation to O* and CO* association and finally to O_2* and CO* association is further disclosed by lowering the CO coverage to achieve a trade-off between elementary steps. Accordingly, a de novo strategy, which starts from the metal–support interfacial charge to the reaction mechanism, kinetics, and thermodynamics of RDS and ultimately leads to catalytic performance, is developed to quantitatively map the CO activation picture with a 10-fold increase in reaction rate. The proposed mechanistic and kinetic picture, together with the de novo strategy, is expected to become a foundation for elucidating EMSIs in heterogeneous catalysis.

Declaration of Competing Interest

The authors declare that they have no conflicts of interest in this work.

Acknowledgments

This work was supported by grants from the Natural Science Foundation of China (Grants No. 21922803, 22178100, 92034301, 22008066, and 21776077), the China Postdoctoral Science Foundation (Grant No. BX20190116), the Innovation Program of Shanghai Municipal Education Commission, the Program of Shanghai Academic/Technology Research Leader (Grant No. 21XD1421000), 111 Project of the Ministry of Education of China (Grant No. B08021). The authors thank beamline BL14W1 (Shanghai Synchrotron Radiation Facility) for the beam time and assistance in the experiments.

Supplementary materials

Supplementary material associated with this article can be found, in the online version, at doi:10.1016/j.fmre.2022.06.012.

References

[1] J.K. Nørskov, T. Bligaard, J. Rossmeisl, et al., Towards the computational design of solid catalysts, Nat. Chem. 1 (2009) 37–46.
[2] T.W. van Deelen, C. Hernández Mejía, K.P. de Jong, Control of metal-support interactions in heterogeneous catalysts to enhance activity and selectivity, Nat. Catal. 2 (2019) 955–970.
[3] H. Fang, J. Yang, M. Wen, et al., Nanoalloy materials for chemical catalysis, Adv. Mater. 30 (2018) 1705698.
[4] Y. Shi, Z.R. Ma, Y.Y. Xiao, et al., Electronic metal-support interaction modulates single-atom platinum catalysis for hydrogen evolution reaction, Nat. Commun. 12 (2021) 3021.
[5] Y. Sun, Z. Xue, Q. Liu, et al., Modulating electronic structure of metal-organic frameworks by introducing atomically dispersed Ru for efficient hydrogen evolution, Nat. Commun. 12 (2021) 1369.
[6] Z. Li, S. Ji, Y. Liu, et al., Well-defined materials for heterogeneous catalysis: from nanoparticles to isolated single-atom sites, Chem. Rev. 120 (2019) 623–682.
[7] F. Calle-Vallejo, D. Loffreda, M.T. Koper, et al., Introducing structural sensitivity into adsorption–energy scaling relations by means of coordination numbers, Nat. Chem. 7 (2015) 403–410.
[8] C.T. Campbell, Electronic perturbations, Nat. Chem. 4 (2012) 597–598.
[9] J. Yang, W.H. Li, S. Tan, et al., The electronic metal–support interaction directing the design of single atomic site catalysts: Achieving high efficiency towards hydrogen evolution, Angew. Chem. 133 (2021) 19233–19239.
[10] H. Zhang, C. Wang, H.L. Sun, et al., In situ dynamic tracking of heterogeneous nanocatalytic processes by shell-isolated nanoparticle-enhanced Raman spectroscopy, Nat. Commun. 8 (2017) 15447.
[11] T. Chen, V.O. Rodionov, Controllable catalysis with nanoparticles: Bimetallic alloy systems and surface adsorbates, ACS Catal 6 (2016) 4025–4033.
[12] A.D. Allian, K. Takanabe, K.L. Fujdala, et al., Chemisorption of CO and mechanism of CO oxidation on supported platinum nanoclusters, J. Am. Chem. Soc. 133 (2011) 4498–4517.
[13] H.J. Freund, G. Meijer, M. Scheffler, et al., CO oxidation as a prototypical reaction for heterogeneous processes, Angew. Chem. Int. Ed. 50 (2011) 10064–10094.
[14] B.M. Weckhuysen, Preface: recent advances in the in-situ characterization of heterogeneous catalysts, Chem. Soc. Rev. 39 (2010) 4557–4559.
[15] U. Bentrup, Combining in situ characterization methods in one set-up: looking with more eyes into the intricate chemistry of the synthesis and working of heterogeneous catalysts, Chem. Soc. Rev. 39 (2010) 4718–4730.
[16] C. Ledesma, J. Yang, D. Chen, et al., Recent approaches in mechanistic and kinetic studies of catalytic reactions using SSITKA technique, ACS Catal 4 (2014) 4527–4547.
[17] A.H. Motagamwala, J.A. Dumesic, Microkinetic modeling: a tool for rational catalyst design, Chem. Rev. 121 (2020) 1049–1076.
[18] G. Kresse, J. Hafner, Ab initio molecular dynamics for liquid metals, Phys. Rev. B 47 (1993) 558–561.
[19] G. Kresse, J. Hafner, Ab initio molecular-dynamics simulation of the liquid-metal-amorphous-semiconductor transition in germanium, Phys. Rev. B 49 (1994) 14251–14269.
[20] G. Kresse, J. Furthmuller, Efficiency of ab-initio total energy calculations for metals and semiconductors using a plane-wave basis set, Comp. Mater. Sci. 6 (1996) 15–50.
[21] G. Kresse, J. Furthmuller, Efficient iterative schemes for ab initio total-energy calculations using a plane-wave basis set, Phys. Rev. B 54 (1996) 11169–11186.
[22] J.P. Perdew, K. Burke, M. Ernzerhof, Generalized gradient approximation made simple, Phys. Rev. Lett. 77 (1996) 3865–3868.
[23] S. Grimme, J. Antony, S. Ehrlich, et al., A consistent and accurate ab initio parametrization of density functional dispersion correction (DFT-D) for the 94 elements H-Pu, J. Chem. Phys. 132 (2010) 154104.
[24] T. Thonhauser, V.R. Cooper, S. Li, et al., Van der Waals density functional: Self-consistent potential and the nature of the van der Waals bond, Phys. Rev. B 76 (2007) 125112.
[25] H.J. Monkhorst, J.D. Pack, Special points for Brillouin-zone integrations, Phys. Rev. B 13 (1976) 5188–5192.
[26] J.R. Feng, G.C. Wang, Theoretical insight into the role of nitrogen in the formic acid decomposition over Pt13/N-GNS, Appl. Surf. Sci. 539 (2021) 148192.
[27] P.E. Blochl, O. Jepsen, O.K. Andersen, Improved tetrahedron method for Brillouin–zone integrations, Phys. Rev. B 49 (1994) 16223–16233.
[28] G. Henkelman, A. Arnaldsson, H. Jonsson, A fast and robust algorithm for Bader decomposition of charge density, Comp. Mater. Sci. 36 (2006) 354–360.
[29] E. Sanville, S.D. Kenny, R. Smith, et al., Improved grid-based algorithm for Bader charge allocation, J. Comp. Chem. 28 (2007) 899–908.
[30] M. Döntgen, M.D. Przybylski-Freund, L.C. Kröger, et al., Automated discovery of reaction pathways, rate constants, and transition states using reactive molecular dynamics simulations, J. Chem. Theory Comput. 11 (2015) 2517–2524.
[31] A.C.T. van Duin, S. Dasgupta, F. Lorant, et al., Reaxff: a reactive force field for hydrocarbons, J. Phys. Chem. A 105 (2001) 9396–9409.
[32] M. Wei, S. Wu, Q. Mao, et al., The oxidation mechanism investigation of benzene catalyzed by palladium nanoparticle: A ReaxFF molecular dynamics, Fuel 275 (2020) 117989.
[33] B.V. Merinov, J.E. Mueller, A.C.T. van Duin, et al., ReaxFF reactive force-field modeling of the triple-phase boundary in a solid oxide fuel cell, J. Phys. Chem. Lett. 5 (2014) 4039–4043.
[34] K.D. Nielson, A.C. van Duin, J. Oxgaard, et al., Development of the ReaxFF re4active force field for describing transition metal catalyzed reactions, with application to the initial stages of the catalytic formation of carbon nanotubes, J. Phys. Chem. A 109 (2005) 493–499.
[35] J. Tersoff, Empirical interatomic potential for carbon, with applications to amorphous carbon, Phys. Rev. Lett. 61 (1988) 2879–2882.
[36] J. Tersoff, New empirical approach for the structure and energy of covalent systems, Phys. Rev. B 37 (1988) 6991–7000.
[37] L. Martínez, R. Andrade, E.G. Birgin, et al., Packmol: a package for building initial configurations for molecular dynamics simulations, J. Comput. Chem. 30 (2009) 2157–2164.
[38] J.M. Martínez, L. Martínez, Packing optimization for automated generation of complex system's initial configurations for molecular dynamics and docking, J. Comput. Chem. 24 (2003) 819–825.
[39] Y.K. Shin, L. Gai, S. Raman, et al., Development of a ReaxFF reactive force field for the Pt-Ni alloy catalyst, J. Phys. Chem. A 120 (2016) 8044–8055.
[40] M. Feng, X.Z. Jiang, K.H. Luo, A reactive molecular dynamics simulation study of methane oxidation assisted by platinum/graphene-based catalysts, P. Combust. Inst. 37 (2019) 5473–5480.
[41] S. Plimpton, Fast parallel algorithms for short-range molecular dynamics, J. Comput. Phys. 117 (1995) 1–19.
[42] A.C. Van Duin, A. Strachan, S. Stewman, et al., ReaxFFSiO reactive force field for silicon and silicon oxide systems, J. Phys. Chem. A 107 (2003) 3803–3811.

[43] A. Sadezky, H. Muckenhuber, H. Grothe, et al., Raman microspectroscopy of soot and related carbonaceous materials: spectral analysis and structural information, Carbon 43 (2005) 1731–1742.
[44] S. Fang, X. Zhu, X. Liu, et al., Uncovering near-free platinum single-atom dynamics during electrochemical hydrogen evolution reaction, Nat. Commun. 11 (2020) 1029.
[45] Y.S. Lee, J.Y. Rhee, C.N. Whang, et al., Electronic structure of Co-Pt alloys: X-ray spectroscopy and density-functional calculations, Phys. Rev. B 68 (2003) 235111.
[46] X. Song, L. Huang, W. He, et al., Electronic Metal–support interactions between Pt nanoparticles and $Co(OH)_2$ flakes for CO Oxidation, J. Phys. Chem. C 123 (2019) 10907–10916.
[47] W. Chen, J. Cao, J. Yang, et al., Molecular-level insights into the electronic effects in platinum-catalyzed carbon monoxide oxidation, Nat. Commun. 12 (2021) 6888.
[48] J.M. Martinez de la Hoz, P.B. Balbuena, Small-molecule activation driven by confinement effects, ACS Catal 5 (2015) 215–224.

Wenyao Chen received B.S. and Ph.D. degrees from East China University of Science and Technology (ECUST) in 2013 and 2018, respectively. After a stay as post-doctoral fellow at University of Toronto, Canada, he joined the faculty of the State Key Laboratory of Chemical Engineering at ECUST. His current research interests include kinetics-assisted design and manipulation of metal catalysts for energy conversion.

Xuezhi Duan received his Ph.D. degree in chemical engineering from East China University of Science and Technology (ECUST) in 2012. After a two-year (2013-2015) stint as post-doctoral fellow at Norwegian University of Science and Technology, he joined the faculty of School of Chemical Engineering at ECUST. He is now a full professor and deputy director of the State Key Laboratory of Chemical Engineering. His current research interests include kinetics-assisted catalyst design, theoretical calculations and reactor engineering. In addition, he received the Young Scientist Prize awarded by the International Association of Catalysis Societies, the Outstanding Youth Award of Global Chinese Chemical Engineers Symposium, the Henry Fok Youth Teacher Award, the Chinese Chemical Society Young Chemist Award, etc.